The Astrophysical Journal Letters, 723:L127–L133, 2010 November 10 doi:10.1088/2041-8205/723/2/L127


# Sunrise: Instrument, Mission, Data, and First Results

S. K. Solanki[1,2], P. Barthol[1], S. Danilovic[1], A. Feller[1], A. Gandorfer[1], J. Hirzberger[1], T. L. Riethmüller[1], M. Schüssler[1], J. A. Bonet[3], V. Martínez Pillet[3], J. C. del Toro Iniesta[4], V. Domingo[5], J. Palacios[5], M. Knölker[6], N. Bello González[7], T. Berkefeld[7], M. Franz[7], W. Schmidt[7], and A. M. Title[8]

[1] Max-Planck-Institut für Sonnensystemforschung, Max-Planck-Str. 2, 37191 Katlenburg-Lindau, Germany; solanki@mps.mpg.de
[2] School of Space Research, Kyung Hee University, Yongin, Gyeonggi 446-701, Republic of Korea
[3] Instituto de Astrofísica de Canarias, C/Via Láctea s/n, 38200 La Laguna, Tenerife, Spain
[4] Instituto de Astrofísica de Andalucía (CSIC), Apdo. de Correos 3004, E-18080, Granada, Spain
[5] Grupo de Astronomía y Ciencias del Espacio, Universidad de Valencia, E-46980, Paterna, Valencia, Spain
[6] High Altitude Observatory, National Center for Atmospheric Research, P.O. Box 3000, Boulder, CO 80307-3000, USA[9]
[7] Kiepenheuer-Institut für Sonnenphysik, Schöneckstr. 6, 79104 Freiburg, Germany
[8] Lockheed-Martin Solar and Astrophysical Lab., Palo Alto, CA 94304, USA
*Received 2010 June 16; accepted 2010 July 1; published 2010 October 15*

## ABSTRACT

The Sunrise balloon-borne solar observatory consists of a 1 m aperture Gregory telescope, a UV filter imager, an imaging vector polarimeter, an image stabilization system, and further infrastructure. The first science flight of Sunrise yielded high-quality data that revealed the structure, dynamics, and evolution of solar convection, oscillations, and magnetic fields at a resolution of around 100 km in the quiet Sun. After a brief description of instruments and data, the first qualitative results are presented. In contrast to earlier observations, we clearly see granulation at 214 nm. Images in Ca II H display narrow, short-lived dark intergranular lanes between the bright edges of granules. The very small-scale, mixed-polarity internetwork fields are found to be highly dynamic. A significant increase in detectable magnetic flux is found after phase-diversity-related reconstruction of polarization maps, indicating that the polarities are mixed right down to the spatial resolution limit and probably beyond.

*Key words:* Sun: chromosphere – Sun: faculae, plages – Sun: photosphere – techniques: photometric – techniques: polarimetric – techniques: spectroscopic

*Online-only material:* animations

## 1. INTRODUCTION

In order to understand processes that govern solar activity, we must disentangle how the magnetic field interacts with the solar plasma and guides the conversion of energy between its mechanical, magnetic, radiative, and thermal forms.

The photosphere represents the key interaction region: thermal, kinetic, and magnetic energy all are of the same order of magnitude and most easily transform from one form into another. This interaction in turn leads to the creation of a rich variety of magnetic structures, from sunspots down to intense magnetic field concentrations on a length scale of 100 km or less. This structuring provides the need to obtain data with a homogeneous and constant resolution of such length scales. One possibility to fulfill this requirement is to fly a telescope carried by a stratospheric balloon.

Balloon missions aiming at high-resolution solar studies have a long history. An early highlight was the 12 inch Stratoscope, which flew multiple times in 1957 (Schwarzschild 1959) and 1959 (Danielson 1961). It produced high-resolution images of solar granulation, the solar limb, and of sunspot fine structure, which for many years represented the state of the art. A similar-sized instrument equipped with a spectrometer, the Spectrostratoscope, flew in 1975, but mainly obtained imaging data of solar granulation (Mehltretter 1976, 1978; Wittmann & Mehltretter 1977). The Soviet Stratospheric Solar Station had multiple flights (e.g., Krat et al. 1970). The 50 cm telescope provided nearly diffraction-limited broadband images of solar granulation and a sunspot (Krat et al. 1972). These data led Karpinsky (1989) to propose large-scale restructuring of the solar granulation on a short time scale. The 80 cm diameter Flare Genesis telescope, equipped with a sophisticated Fabry–Pérot-based vector magnetograph (Rust et al. 1996), flew in 1996 and 2000, achieving a spatial resolution of roughly 0.5 arcsec (Georgoulis et al. 2002) during the second flight. This experiment resulted in the discovery of bipolar magnetic features moving toward a very young sunspot, which were interpreted as small U-loops (Bernasconi et al. 2002; Georgoulis et al. 2002).

In addition to achieving high resolution, stratospheric balloon flights also allow the Sun to be explored in near-ultraviolet radiation that is strongly attenuated by Earth's atmosphere. In 1970 and 1971, a 20 cm telescope flew on a stratospheric balloon and recorded images between 200 nm and 460 nm (Hersé 1979). Later, the Rasolba balloon experiment, a 30 cm telescope with an ultraviolet spectrograph, obtained high-resolution spectra in the wavelength range between 190 nm and 295 nm, which includes the Mg II h and k lines (Samain & Lemaire 1985; Staath & Lemaire 1995).

Sunrise extends this tradition of telescopes carried by a stratospheric balloon in order to study the Sun. It combines high spatial resolution with sensitivity to ultraviolet radiation. At 1 m diameter, it is the largest solar telescope so far to leave the ground. It is equipped with sophisticated post-focus instruments, including a UV imager and a filter-based vector magnetograph.

[9] HAO/NCAR is sponsored by the NSF.

## 2. INSTRUMENTATION AND MISSION

### 2.1. Instrument

The SUNRISE stratospheric balloon-borne observatory is composed of a telescope, two post-focus science instruments (SuFI and IMaX, see below), an Image Stabilization and Light Distribution (ISLiD) unit, and a Correlating Wavefront Sensor (CWS), carried in a gondola, which possesses pointing capability.

#### 2.1.1. Telescope

The telescope is a Gregory-type reflector with 1 m clear aperture and an effective focal length of close to 25 m. A heat-rejection wedge at the prime focus reflects 99% of the light from the solar disk off to the side, reducing the heat load on the post-focus instruments to approximately 10 W. The secondary mirror is actively controlled in three degrees of freedom to compensate for thermoelastic deformations of the telescope during flight. The post-focus instrumentation rests on top of the telescope. More details are given by Barthol et al. (2010).

#### 2.1.2. SuFI

The SUNRISE Filter Imager (SuFI) provides images at violet and near ultraviolet wavelengths. The wavelengths sampled by SuFI are 214 nm at 10 nm bandwidth, 300 nm at 5 nm bandwidth, 312 nm at 1.2 nm bandwidth, 388 nm at 0.8 nm bandwidth, and 396.8 nm (core of Ca II H) at 0.18 nm bandwidth. A 2048 × 2048 UV-enhanced CCD is employed, with a plate scale of 0.02 arcsec pixel$^{-1}$, on average (the plate scale is slightly wavelength dependent). In order to overcome aberrations due to thermoelastic deformations of the telescope and any remaining seeing, a phase-diversity technique (cf. Paxman et al. 1992; Löfdahl & Scharmer 1994) is used: a special optical arrangement in front of the detector delivers a nominally focused image on one half of the detector, while the other half receives an image with a defocus of one wave at 214 nm. Hence, the field of view (FOV) is 15 × 40 arcsec$^2$. Both halves of the CCD together provide sufficient information for post-facto removal of low-order aberrations from the image.

A cadence of better than an image every 2 s can be achieved, depending on the exposure time, to either take rapid time series at a given wavelength or to switch wavelengths. Thus, the four longer wavelengths can be cycled through within 8 s. Since the exposure time of the 214 nm was typically 30 s even at local noon, owing to residual ozone at and above float altitudes, the cadence was correspondingly lower whenever this wavelength was included.

A description of SuFI can be found in Gandorfer et al. (2010).

#### 2.1.3. IMaX

The Imaging Magnetograph eXperiment (IMaX) operates in the Fe I 525.02 nm line (a Zeeman triplet with Landé factor $g = 3$). Images in polarized light covering 50 × 50 arcsec$^2$ are recorded at a spectral resolution of 85 m Å, normally at four wavelengths within the spectral line and one in the nearby continuum. The full Stokes vector in these five wavelengths at a noise level of $10^{-3}$ is obtained in 30 s, which is the typical cadence for most of the observations. The number of wavelength points (between 3 and 12) and of polarization states can be varied to obtain a higher cadence, or a better rendering of the line profile shape.

The spectral resolution and sampling is achieved by using a thermally stabilized tunable solid-state Fabry–Pérot etalon in double pass together with a narrowband, prefilter with an FWHM of 0.1 nm.

Polarization states are isolated with the help of two nematic liquid-crystal modulators operated at a frequency of 4 Hz, which are switched between four states for full Stokes vector polarimetry. A dual-beam approach is taken, with two synchronized 1k×1k CCD cameras. After every observing run, a plate is inserted into the light path in front of one of the cameras in order to obtain phase-diversity information for post-facto reconstruction. Detailed information on IMaX is provided by Martínez Pillet et al. (2010).

#### 2.1.4. ISLiD

The Image Stabilization and Light Distribution (ISLiD) unit allows simultaneous observations with the two science instruments by distributing the radiation according to wavelength (200–400 nm to SuFI; 525 nm to IMaX; 500 nm to CWS), while preserving diffraction-limited performance as well as polarization information. ISLiD contains a rapid, piezo-driven tip-tilt mirror, which stabilizes the image on the science instrument foci by damping all vibrations and motions acting at frequencies up to 60 Hz. This mirror is controlled by CWS, which is optically stimulated by ISLiD. ISLiD is described by Gandorfer et al. (2010).

#### 2.1.5. CWS

The Correlating Wavefront Sensor (CWS) is a Shack–Hartmann-type wavefront sensor with a lenslet array in a pupil image that feeds an FOV of 12 × 12 arcsec$^2$ on a high-speed camera. It is used in two ways: as a fast correlation tracker to derive control signals for a tip-tilt mirror and as a slow wavefront sensor (defocus and coma) for active alignment control of the telescope secondary mirror. The CWS is described by Berkefeld et al. (2010).

#### 2.1.6. Gondola

The SUNRISE gondola provides the housing for the telescope, instruments, power supply, etc. In addition, it is responsible for the precision pointing of the telescope toward the Sun. Situated approximately 100 m below the drifting balloon, the gondola attitude control system nominally keeps the telescope orientation fixed to the Sun within a range of less than ±45 arcsec. Within this range, ISLiD and CWS are able to compensate for residual motions and allow continuous observations. Azimuthal control of the gondola is performed via a momentum transfer unit at its top.

Electrical power is provided by large photovoltaic arrays housed in two panels placed left and right of the telescope. On the rear side of the gondola, the instrument control electronics are mounted on two racks.

The two data storage containers collecting the science data are securely mounted inside one of the upper side trusses of the core framework, which provides protection and easy access for data recovery after landing. The complete payload has dimensions of 5.5 m in width and length, is about 6.4 m high, and has a mass of 1919.6 kg (without Columbia Scientific Ballooning Facility (CSBF) equipment, ballast, etc.). More information on the gondola is provided by Barthol et al. (2010).

### 2.2. Mission

SUNRISE was flown on a zero-pressure stratospheric long-duration balloon, launched and operated by the CSBF. It was

**Table 1**
SuFI Observing Modes

| SuFI Mode | Fraction of Observing Time |
|---|---|
| 5λ: 214, 300, 312, 388, 397 nm | 8% |
| 4λ: 300, 312, 388, 397 nm | 56% |
| 3λ: 300, 388, 397 nm | 9% |
| 2λ: mostly 388, 397 nm | 12% |
| 1λ: mostly 397 nm | 15% |

launched on 2009 June 8 at 6:27 UT (08:27 h local time) from ESRANGE (67.89N, 21.10E) near Kiruna in northern Sweden. It then floated westward at a mean cruise altitude of 36 km and landed on Somerset island (northern Canada), suspended on a parachute, on 2009 June 13 at 23:47 UT. The payload remained in direct sunlight during the entire flight. Since at float altitudes the payload was above 99% of the Earth's atmosphere, virtually seeing-free observations were possible all the time. Also, the balloon stayed above most of the ozone in Earth's atmosphere, allowing high-resolution imaging in the UV at 214 nm, 300 nm, and 312 nm.

The loss of high-speed telemetry relatively soon after reaching float altitude (due to the failure of a rented commercial telemetry system) meant that no full images could be downloaded during the entire mission, so that instrument commissioning and operations had to be carried out practically blindly.

## 3. OVERVIEW OF THE DATA RECORDED DURING THE 2009 FLIGHT OF SUNRISE

The total observation time was 130 hr, in which IMaX acquired 415 GB of data (480332 images) and SuFI recorded 790 GB (150288 images). 55685 of the SuFI images were acquired while the CWS control loop was closed. 16128 of these closed-loop images were collected near or at the solar limb ($\mu < 0.5$).

During 23% of the total time at float altitude the CWS loop was closed. We obtained continuous time series longer than 1 minute during 22% and time series longer than 10 minutes during 10% of the total observation time. The longest time series of SuFI data is 34 minutes, but only 19 minutes for the SuFI mode that includes the shortest wavelength of 214 nm. This wavelength is by far the most sensitive to the airmass along the line of sight (LOS) and was only observed around local noon. The longest IMaX time series lasts 32 minutes.

During data reduction, different versions of SuFI data are generated. Starting from the level-0 raw data, level-1 data are produced that are fully reduced, but not phase-diversity reconstructed. A first phase-diversity reconstruction using individual wavefronts for each image results in level-2 data. Finally, level-3 data are phase-diversity reconstructed employing an averaged wavefront (see Hirzberger et al. 2010b for more details on SUNRISE/SuFI data reduction). A brief summary of the recorded SuFI data is given in Tables 1 and 2.

IMaX observed in various modes that differ in the number of Stokes parameters observed, or the number of wavelength points, or the number of integrations at each wavelength, or some combination of these three parameters. They are designated by the following nomenclature: letter L or V (L = longitudinal, i.e., only Stokes $I$ and $V$ are observed, V = vector, i.e., full Stokes vector observed) followed by the number of wavelength points (3, 5, and 12 were used on this flight) and the number of integrations per wavelength. The most widely used ("standard") mode is V5-6, i.e., Stokes vector measured in five wavelengths (four in the line and one in the continuum), with six images accumulated per wavelength point. The cadence of the observations, the achieved noise level, and the amount of time for which each mode was observed is given in Table 3. Note that the noise level refers to the Stokes $I$ continuum and is given for the unreconstructed data. After reconstruction, the noise level increases by roughly a factor of three. The effective spatial resolution of the reconstructed data at 0.15–0.18 arcsec, however, is considerably higher and results in the resolution of both, small-scale magnetic and convective features (Lagg et al. 2010; Khomenko et al. 2010).

**Table 2**
SuFI Exposure Times and Numbers of Images

| Central λ (nm) | Exp. Time $\mu \geqslant 0.5$ (ms) | Exp. Time $\mu < 0.5$ (ms) | No. Images $\mu \geqslant 0.5$ | No. Images $\mu < 0.5$ |
|---|---|---|---|---|
| 214 | 30000 | 30000 | 409 | 33 |
| 300 | 100–500 | 200–800 | 8949 | 2649 |
| 312 | 100–500 | 200–800 | 7372 | 2662 |
| 388 | 60–150 | 65–210 | 11560 | 2992 |
| 396.8 | 250–1200 | 750–1500 | 11267 | 7792 |
| Σ | | | 39557 | 16128 |

**Table 3**
Time Spans and Cadences of Various IMaX Modes

| Date Mode | Cadence (s) | Noise ($I_c$) | Total (minutes) |
|---|---|---|---|
| V5-6 | 33 | 0.0011 | 553 |
| V5-3 | 18 | 0.0015 | 180 |
| V3-6 | 20 | 0.0011 | 13 |
| L12-2 | 31 | 0.0013 | 64 |
| L3-2 | 8 | 0.0013 | 42 |

The reduction of IMaX data and the various calibrations of the instrument are described by Martínez Pillet et al. (2010). Different versions of IMaX data are produced. These include level-0 raw data, level-1 fully reduced, but not the reconstructed data and level-2 data, which were reconstructed by deconvolution using a modified Wiener filter and the point-spread function of the optical system derived from calibration applying phase diversity. The reconstruction of the IMaX data always makes use of an averaged wavefront, so that IMaX level-2 data correspond to SuFI level-3 data.

## 4. FIRST RESULTS

The Sun was extremely quiet during the entire flight of SUNRISE, so that almost all of the SUNRISE data correspond to internetwork regions with occasional network elements.

### *4.1. Results from SuFI Data*

Images of the quiet Sun at the disk center in all five SuFI wavelengths are shown in Figure 1(a), whose gray scale is saturated at $\langle I \rangle \pm 3\sigma$ for each wavelength in order to allow a better intercomparison of the granulation, at the cost of overexposing the bright points (BPs; this figure shows the same solar scene as Figure 13 of Gandorfer et al. 2010, but with a different brightness scaling). The brightness scale (see the gray-scale bars above the individual frames) already indicates the large rms contrasts of the imaged granulation (see Hirzberger et al. 2010a, for a quantitative analysis). The images at 300 nm, 312 nm, and 388 nm display rather similar granulation patterns

and prominent BPs, especially in the network feature near the center of the frame. Even in the 214 nm image, granulation is well identified, although intergranular lanes are no longer that clearly visible. It cannot be completely ruled out, however, that this is due to a larger spatial smearing. In addition, the granules display more substructure in the 214 nm images. This is in contrast to the statement made by Hersé (1979) that "at λ200 nm we find only bright grains of a mean area of 4 arcsec$^2$ and a mean contrast of 47%." Hersé identified them with facular grains. The reason for the difference may partly lie in strong underexposure of the granulation (see his Figures 4 and 5). There is a hint of granule-like structures in the lower right part of his Figure 7 (only visible in the printed paper).

BPs are particularly prominent at 214 nm (their contrasts are highest at this wavelength; see Riethmüller et al. 2010), but somewhat more diffuse. This may be due to image jitter accumulated during the 30 s exposure and the greater height of formation of this wavelength, combined with the expansion of magnetic features with height.

Ca II H 397 nm displays a variety of features including reversed granulation, oscillations and waves, and magnetic BPs. The leftmost frame of Figure 1(a) reveals that although many of the intergranular lanes are indeed bright, some appear as dark stripes with bright lanes on either side of them. Examples can be found extending between the coordinates (4, 1) and (5, 3), from (4, 4) to (3, 7), or from (5, 8) to (8, 7). Time series of Ca II H images (see Animation 1 available in the online edition of the journal) reveals that these dark Ca II H lanes are rather short lived. Possibly they are a result of the interaction of the reversed granulation with waves.

At an intermediate heliocentric angle of $\mu = \cos\theta$ of roughly 0.72 (not shown) the granulation appears very similar at 300, 312, and 388 nm. At 214 nm, however, structures intermediate between reversed and normal granulation appear, with bright lanes (on the centerward side) and darker granule bodies.

One interpretation of the different behavior displayed by 214 nm data is that the radiation in this band is formed (on average) at a greater height. A rough estimate, made including line opacities, can be obtained from Figure 1 of Vernazza et al. (1976). It shows that around 300 nm the radiation is formed roughly 50 km above $\tau_{500\mathrm{nm}} = 1$, while at 214 nm it is formed around 250 km above $\tau_{500\mathrm{nm}} = 1$. The true value at 214 nm is rather tricky to determine owing to the broad filter profile, the presence of the ionization edge of aluminum within the filter range, and the great density of spectral lines at these wavelengths. Thus, the analysis of Solanki & Unruh (1998) suggests a lower formation height of ∼100 km above $\tau_{500\mathrm{nm}} = 1$. We speculate that 214 nm wavelength radiation is formed sufficiently high in the atmosphere that first signs of reversed granulation become visible at the disk center (e.g., filling in of intergranular lanes in Figure 1(a)). As we move toward the limb, the reversed granulation becomes more apparent.

Reversed granulation is seen clearly in Ca II H, but many of the finer-scale features are lost. The intermediate nature of 214 nm is illustrated by the fact that the best correspondence of 397 nm is found with 214 nm (coherence values are a factor of 1.5 higher than those between, e.g., 300 nm and 397 nm).

Images at four SuFI wavelengths at the solar limb in the general vicinity of the south solar pole are shown in Figure 1(b). Obviously the structures at the south limb, although reminiscent of granules, are considerably smaller than those further away from the limb, in qualitative agreement with earlier results (Sánchez Cuberes et al. 2003). This smaller size could be related to greater prominence of granular substructure at the limb. In addition, polar faculae are visible, e.g., around $y = 13$, 20, and 36. Fibrils can be seen emanating from the faculae at $y \approx 13$ and spicules are clearly present off the solar limb (they became visible after the off-limb brightness was enhanced). Some of the spicule-like structures appear strongly inclined to the vertical and even slightly bent, so that they may actually be parts of quiet-Sun loops.

### 4.2. Results from IMaX Data

Figure 2 shows a snapshot of IMaX data products; clockwise from upper left: continuum intensity, LOS velocity, total net linear polarization averaged over the line, $L_s$, and the similarly averaged Stokes $V$, $V_s$ (see below). All quantities are based on the reconstructed data, with the exception of $L_s$, for which the unreconstructed data are shown (reconstruction increases the noise, so that a number of significant $L_s$ patches in the unreconstructed image are no longer sufficiently above the noise in the reconstructed data). $V_s$ and $L_s$ are defined as

$$V_s = \frac{1}{4\,\langle I_c\rangle}\sum_{i=1}^{4} a_i V_i \quad \text{and} \quad L_s = \frac{1}{4\,\langle I_c\rangle}\sum_{i=1}^{4}\sqrt{Q_i^2 + U_i^2}.$$

Here, $i$ runs over the four wavelength points inside the spectral line, $a_i$ takes on values of $1, 1, -1, -1$ for $i = 1$–4 (see Martínez Pillet et al. 2010), and $\langle I_c\rangle$ is the continuum intensity averaged over the FOV.

The rms contrast of quiet-Sun granulation obtained from IMaX continuum data is around 13.5%, which is a mark of the outstanding quality of the IMaX images. Due to the longer wavelength at which IMaX observes, the contrast is lower than that in the SuFI images. In particular, the BPs are less clearly visible, having a contrast comparable to that of granulation (see Riethmüller et al. 2010). The velocity images prominently display a network of sharp intergranular downflow lanes (appearing bright in the figure). Upflow velocities are often largest in small patches, corresponding to small, often bright granules or parts of larger granules, although there is no one-to-one relationship between upflow speed and brightness (e.g., Hirzberger et al. 2001). In addition, a larger scale velocity pattern composed of 5″–10″ patches superposed on the granulation reflects the $p$-mode oscillations (see Roth et al. 2010 for a detailed analysis of the $p$-modes and Bello González et al. 2010 for a determination of the vertical energy flux transported by high-frequency waves). These enhance the granular downflows and upflows according to the oscillation phase, as can be seen from the time series displayed in Animation 2 (available in the online edition of the journal).

The largest patch of strong Stokes $V$ near the bottom center of the frame is a network element. Other network patches are also present in the frame, but are less prominent, e.g., at (23, 31) in Figure 2. Most of the Stokes $V$ signal, however, is due to internetwork fields. These are clearly composed of rather localized (point-like or crinkled line-like) mixed-polarity magnetic patches. The sizes of internetwork magnetic features deduced from Stokes $V$ are typically below 1″, with many having sizes lying close to the spatial resolution of roughly 0.″15. The internetwork fields clearly outline cell-like structures with "mesogranular" scale sizes (cf. de Wijn et al. 2005, 2008) that range from 2″–3″ in regions with strong internetwork flux to 5″–15″ in regions with particularly low flux. There are hints of

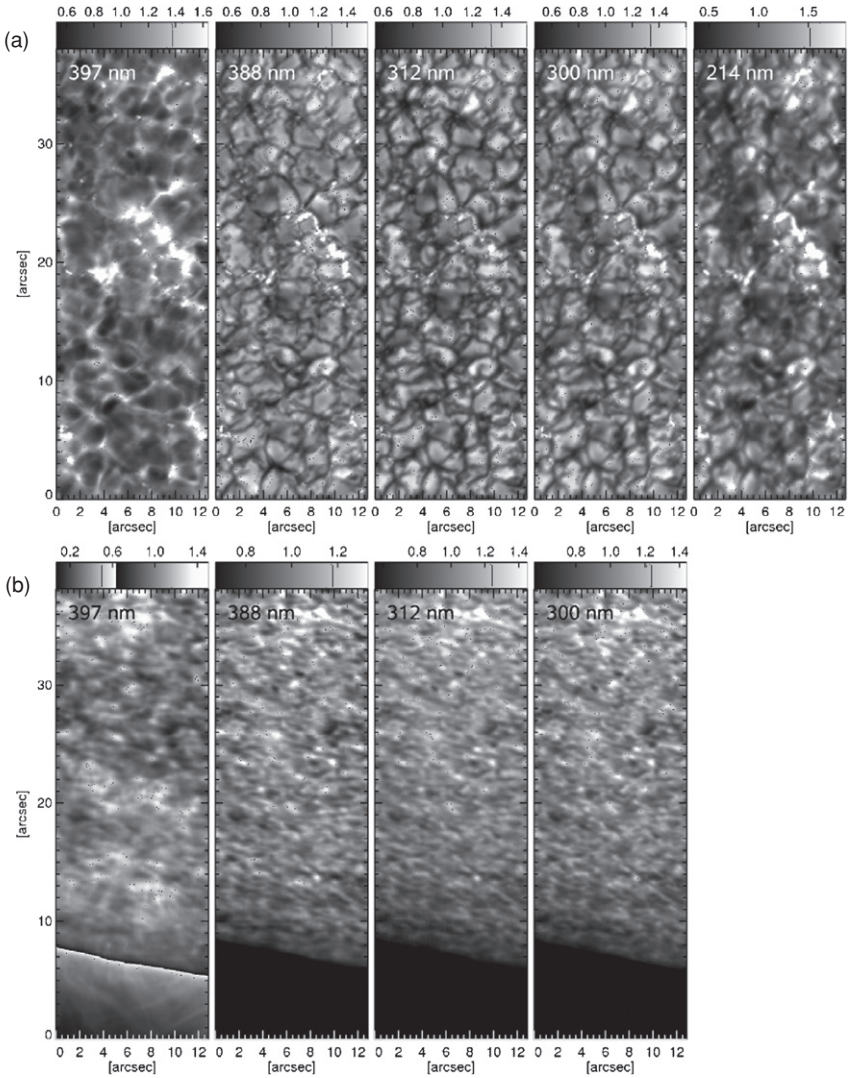


**Figure 1.** (a) Images of a patch of the quiet Sun near the disk center recorded by the SuFI instrument in wavelength bands centered on 397 nm, 388 nm, 312 nm, 300 nm, and 214 nm (from left to right). The gray scale has been individually set to cover three times the rms range of each image. (b) Same as panel (a), but right at the solar limb. The Ca H image (397 nm) is plotted with an enhanced brightness scale for the off-limb parts in order to reveal spicules. Owing to the low-light level, no 214 nm data are available at this position.

smaller cells in such low-flux regions, which, however, cannot be confirmed without an in-depth analysis. At many locations both magnetic polarities are located in close proximity to each other.

$L_s$ displays a meso to supergranular scale pattern. The larger apparent scale of this pattern (compared to that displayed by Stokes $V$) may result from the fact that, on average, $L_s$ features have a lower signal-to-noise ratio than Stokes-$V$ patches, so that we are probably missing more features of the former. The spatial distribution is also different, with the most prominent Stokes-$V$ elements being absent in the linear polarization signal. The opposite is generally not the case. The more prominent patches of linear polarization are usually associated with (weaker) patches of Stokes $V$ (see Danilovic et al. 2010).

Stokes-$V$ movies, such as that displayed in Animation 2, reveal how dynamic the quiet-Sun magnetic field is, with the weaker magnetic features, i.e., those in the internetwork, being particularly dynamic. Constant appearance and disappearance of patches of Stokes $V$ is observed along the edges of the "mesogranular scale" internetwork cells. As pointed out by de Wijn et al. (2008), weaker features often disappear and reappear close by. This could be an effect of features dropping below the noise level by weakening and appearing again as they get more concentrated. However, we also expect the emergence and submergence of magnetic flux to take place on timescales of minutes. This is supported by the analysis of $L_s$. Strong patches of linear polarization are found to be rather short lived and are often associated with bipolar magnetic features suggestive of small-scale loops (Danilovic et al. 2010). Some of these are also associated with supersonic velocities, presumably in the form of upflows (Borrero et al. 2010). There are also locations at which fresh flux emerges in a complex patch of mixed polarities (e.g., Zhang et al. 1998), similar to the simulations of Cheung et al. (2008), but on a small scale. An example in our data is given at around (36, 18) the middle of the time series.

The SUNRISE/IMaX Stokes-$V$ movie displays qualitative similarities to movies of the vertical magnetic field in turbulent dynamo simulations (Vögler & Schüssler 2007), although both the spatial and the temporal scales are quite different. However, both display vortical motions of weak magnetic field patches (see Bonet et al. 2010 for a study of the vortices in these data; cf. Steiner et al. 2010). In the simulations, the mixed-polarity

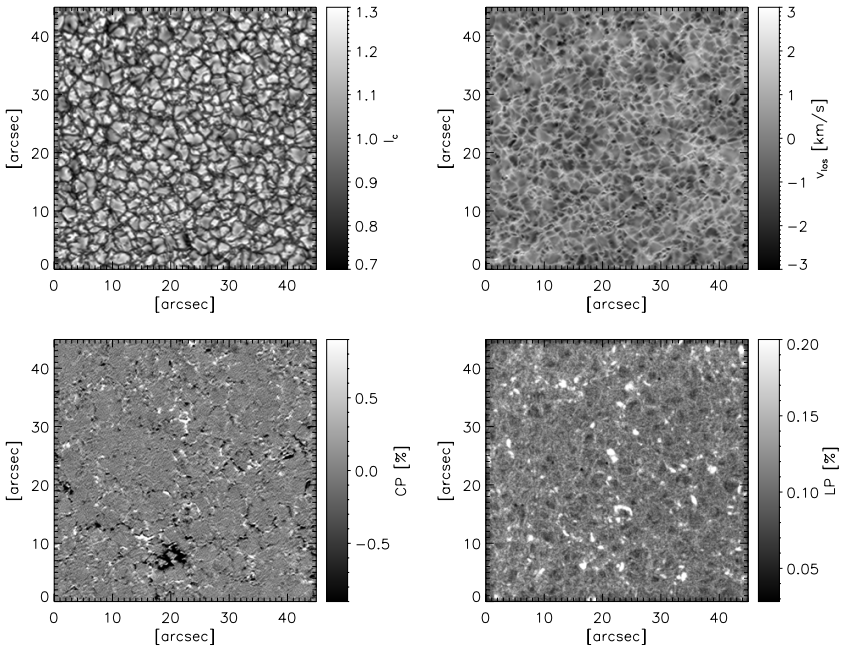


**Figure 2.** IMaX data. Clockwise from upper left: continuum intensity at 5250.4 Å, LOS velocity, net linear polarization $L_s$ (see the text for an exact definition), and line-averaged Stokes $V$, $V_s$ (see the main text for a definition), obtained from Fe I 5250.2 Å. All images are based on the reconstructed data except for the linear polarization image.

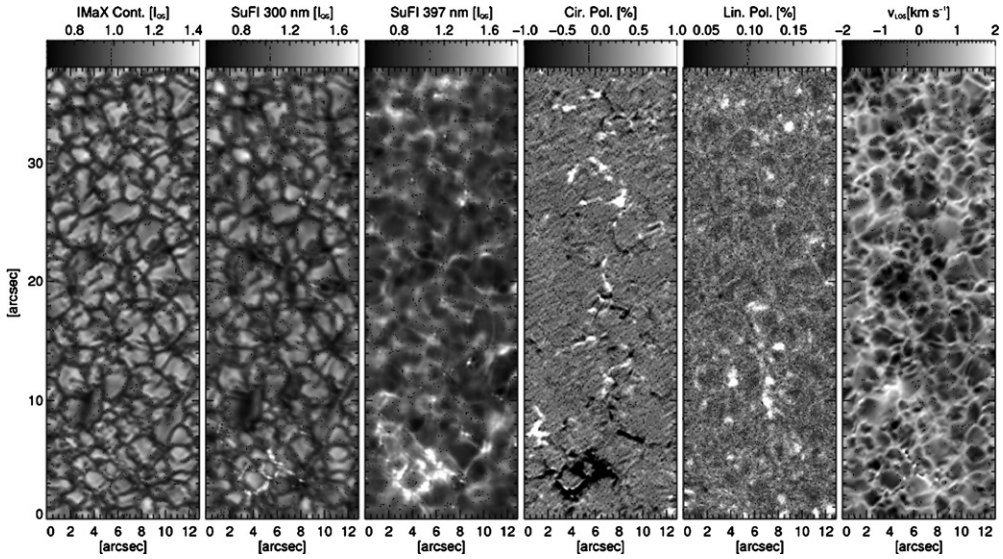


**Figure 3.** Cotemporal SuFI and IMaX data showing the SuFI FOV. From left to right: continuum intensity at 525.04 nm (IMaX data), intensity in the 300 nm band (SuFI data), intensity in the Ca II H line core (SuFI data), net circular polarization deduced from Fe I 525.02 nm (IMaX data), total net linear polarization ($L_s$; IMaX data), and LOS velocity (IMaX). All images have been reconstructed except for the linear polarization image.

magnetic fields are distributed between granules. There the individual magnetic features live less than the granule lifetime. In the observations, both size scales and lifetimes are significantly larger/longer. Quiet-Sun magnetic fields in both, the turbulent dynamo simulations and *Hinode* observations, display a self-similar (fractal) spatial distribution (Pietarila Graham et al. 2009). This supports the idea that structure and evolution over different scales (of our observations and the MHD simulations) are similar.

The unreconstructed Stokes-$V$ map has a noise level of 3.0 G, with a conversion from Stokes $V$ to $B$ following Martínez Pillet et al. (2010). Similarly, the reconstructed map has 9.8 G. The average $V$ above $2\sigma$ in the reconstructed and non-reconstructed maps (i.e., averaged over all pixels, but with the signal set to zero in all pixels with $V < 2\sigma$), converted into LOS field component $B_z$, gives $\langle|B_{z,\mathrm{rec}}|\rangle = 7.31$ G above $2\sigma_{\mathrm{rec}} = 2{\cdot}9.8$ G and $\langle|B_{z,\mathrm{nonrec}}|\rangle = 4.01$ G for $2\sigma_{\mathrm{nonrec}} = 2{\cdot}3.0$ G. The index "rec" implies the reconstructed data and "nonrec" the non-reconstructed data. Thus, in spite of more than three times higher noise, the reconstructed image displays almost twice the amount of magnetic flux. If we set the same limit for both maps, namely, $2\sigma_{\mathrm{rec}}$, then $\langle|B_{z,\mathrm{nonrec}}|\rangle$ is reduced to 1.96 G. This means that 3.7 times more magnetic flux is found if the effective spatial resolution is increased by roughly a factor of two. This difference persists also if the threshold is set higher, so that it cannot be due to contributions from pixels containing noise $>2\sigma$.

This strong increase in magnetic flux suggests that the magnetic polarities are mixed at very small scales approaching

the resolution limit of the present data, so that even moderate additional smearing leads to a substantial decrease in the amount of the visible flux. This dependence on resolution is much stronger than that found for the quiet Sun at lower spatial resolution by Krivova & Solanki (2004), and seemingly also than that found by Pietarila-Graham et al. (2009). Quantitative comparisons are difficult, however, since the reconstruction does not, strictly speaking, change the spatial resolution, but rather significantly enhances the modulation transfer function at frequencies below the cutoff.

The increase in magnetic field strength also implies a considerably higher magnetic energy in the chromosphere (Wiegelmann et al. 2010).

### 4.3. Combination of SuFI and IMaX data

Figure 3 displays a set of cotemporal and cospatial SuFI and IMaX data. Clearly, the prominent, small-scale photospheric BPs in the photospheric SuFI image (second frame from left) are all associated with brightenings in Ca II H and with Stokes-*V* signals, although in some cases these signals are not particularly strong (cf. Riethmüller et al. 2010). Note that in the internetwork these BPs are still very sharp also in Ca II H, which distinguishes them from more wave-like features, which are in general not quite so concentrated. In the 525 nm continuum, however, they are barely detectable. After identifying them in the 300 nm image they can, however, be made out as points with a similar brightness as the surrounding granules.

The relationship between the Ca II H brightness and the magnetic field is more complex. While some of the magnetic features are associated with Ca II H brightenings, e.g., in the network feature near the bottom of the frame, or other magnetic features related to internetwork BPs, there are numerous magnetic features in the internetwork, e.g., at (3.5, 8.5) or between (7.5, 8.5) and (7.5, 11), which are not associated with Ca II H brightenings. Such Ca-dark magnetic features often display mixed polarity and are closely related to patches of $L_s$ (one striking case is discussed by S. Danilovic et al. 2010, in preparation). Conversely, there are numerous Ca II H brightenings which do not seem to have any magnetic counterpart in the photosphere. Examples are at (12, 14) and (10, 22). Although some of them can appear relatively concentrated, on the whole they are clearly more diffuse than the brightenings due to magnetic features. These may correspond to $H_{2V}$ BPs (Rutten & Uitenbroek 1991), although without further spectral information we cannot be sure.

## 5. CONCLUSION

The SUNRISE observatory has provided high-quality, high-resolution images, Dopplergrams, and vector magnetograms at different positions on the solar disk. The extremely low solar activity level at that time means that these data mainly enable new insights into the quiet Sun. Here, we provided a qualitative description of these data and some of the features visible in them. This, together with the more quantitative analyses described in the following SUNRISE papers in this issue, has already led to new insights into the magnetism, convection and oscillations and waves in the quiet Sun. Given the richness and quality of the data and the fact that so far only a very small fraction of them have been analyzed, we expect many more results to follow. A flight of SUNRISE during a period of higher solar activity is greatly to be welcomed.

We thank R. Rutten for helpful discussions on the structure of the chromosphere. The German contribution to SUNRISE is funded by the Bundesministerium für Wirtschaft und Technologie through Deutsches Zentrum für Luft- und Raumfahrt e.V. (DLR), Grant No. 50 OU 0401, and by the Innovationsfond of the President of the Max Planck Society (MPG). The Spanish contribution has been funded by the Spanish MICINN under projects ESP2006-13030-C06 and AYA2009-14105-C06 (including European FEDER funds). The HAO contribution was partly funded through NASA grant number NNX08AH38G. This work has been partially supported by the WCU grant number R31-10016 funded by the Korean Ministry of Education, Science, & Technology.

## REFERENCES

Barthol, P., et al. 2010, Sol. Phys., in press (arXiv:1009.2689)
Bello González, N., et al. 2010, ApJ, 723, L134
Berkefeld, T., et al. 2010, Sol. Phys., in press (arXiv:1009.3196)
Bernasconi, P. N., Rust, D. M., Georgoulis, M. K., & Labonte, B. J. 2002, Sol. Phys., 209, 119
Bonet, J. A., et al. 2010, ApJ, 723, L139
Borrero, J. M., et al. 2010, ApJ, 723, L144
Cheung, M. C. M., Schüssler, M., Tarbell, T. D., & Title, A. M. 2008, ApJ, 687, 1373
Danielson, R. E. 1961, ApJ, 134, 275
Danilovic, S., et al. 2010, ApJ, 723, L149
de Wijn, A. G., Lites, B. W., Berger, T. E., Frank, Z. A., Tarbell, T. D., & Ishikawa, R. 2008, ApJ, 684, 1469
de Wijn, A. G., Rutten, R. J., Haverkamp, E. M. W. P., & Sütterlin, P. 2005, A&A, 441, 1183
Gandorfer, A., et al. 2010, Sol. Phys., in press (arXiv:1009.1037)
Georgoulis, M. K., Rust, D. M., Bernasconi, P. N., & Schmieder, B. 2002, ApJ, 575, 506
Hersé, M. 1979, Sol. Phys., 63, 35
Hirzberger, J., Koschinsky, M., Kneer, F., & Ritter, C. 2001, A&A, 367, 1011
Hirzberger, J., et al. 2010a, ApJ, 723, L154
Hirzberger, J., et al. 2010b, A&A, submitted
Karpinsky, V. N. 1989, Nature, 341, 311
Khomenko, E., et al. 2010, ApJ, 723, L159
Krat, V. A., Karpinsky, V. N., & Pravdjuk, L. M. 1972, Sol. Phys., 26, 305
Krat, V. A., et al. 1970, Astron. Circ., 597, 1
Krivova, N. A., & Solanki, S. K. 2004, A&A, 417, 1125
Lagg, A., et al. 2010, ApJ, 723, L164
Löfdahl, M. G., & Scharmer, G. B. 1994, A&AS, 107, 243
Martínez Pillet, V., et al. 2010, Sol. Phys., in press (arXiv:1009.1095)
Mehltretter, J. P. 1976, Sterne Weltraum, 15, 44
Mehltretter, J. P. 1978, A&A, 62, 311
Paxman, R. G., Schulz, T. J., & Fienup, J. R. 1992, J. Opt. Soc. Am. A, 9, 1072
Pietarila Graham, J., Danilovic, S., & Schüssler, M. 2009, ApJ, 693, 1728
Riethmüller, T. L., et al. 2010, ApJ, 723, L169
Roth, M., et al. 2010, ApJ, 723, L175
Rust, D. M., Murphy, G., Strohbehn, K., & Keller, C. U. 1996, Sol. Phys., 164, 403
Rutten, R. J., & Uitenbroek, H. 1991, Sol. Phys., 134, 15
Samain, D., & Lemaire, P. 1985, Ap&SS, 115, 227
Sánchez Cuberes, M., Vázquez, M., Bonet, J. A., & Sobotka, M. 2003, A&A, 397, 1075
Schwarzschild, M. 1959, ApJ, 130, 345
Solanki, S. K., & Unruh, Y. C. 1998, A&A, 329, 747
Staath, E., & Lemaire, P. 1995, A&A, 295, 517
Steiner, O., et al. 2010, ApJ, 723, L180
Vernazza, J. E., Avrett, E. H., & Loeser, R. 1976, ApJS, 30, 1
Vögler, A., & Schüssler, M. 2007, A&A, 465, L43
Wiegelmann, T., et al. 2010, ApJ, 723, L185
Wittmann, A., & Mehltretter, J. P. 1977, A&A, 61, 75
Zhang, J., Lin, G., Wang, J., Wang, H., & Zirin, H. 1998, A&A, 338, 322